Nanocrystalline transition aluminas: Nanostructure and features of x-ray powder diffraction patterns of low-temperature Al_2O_3 polymorphs

Sergey V. Tsybulya* and Galina N. Kryukova†
Boreskov Institute of Catalysis, SBRAS, Prospekt Lavrentieva 5, Novosibirsk 630090, Russia
(Received 3 May 2007; revised manuscript received 18 October 2007; published 28 January 2008)

Low-temperature γ-, η-, and χ-Al_2O_3 polymorphs were studied by high resolution transmission electron microscopy and x-ray powder diffraction along with computer simulation of the diffraction patterns. Planar defects lying on the {111}, {110}, and {100} planes, which are the origin of the broadening of x-ray diffraction peaks in different forms of aluminium oxide, were revealed. In addition to providing strong experimental support for the imperfect character of the specimen structures, these results demonstrate the possibility of using nanosized crystalline domains with a spinel-type arrangement, which are regularly shaped and have a specified, developed face and bounding surfaces, for the description of the nanostructure of a whole variety of low-temperature Al_2O_3 derivatives. It was found that different ways of domain packing in the oxide particles with a subsequent formation of planar defects contribute to specific kinds of line-shape broadening observed in the x-ray diffraction patterns of these materials. The mechanism of the vacancy generation upon propagation of the shear-type defect in the {110} plane of the spinel structure, which changes the Al_3O_4 stoichiometry to Al_2O_3, is also discussed.

DOI: 10.1103/PhysRevB.77.024112 PACS number(s): 61.72.−y, 81.07.Bc, 68.37.Lp, 61.72.Dd

I. INTRODUCTION

Al_2O_3, traditionally referred to as alumina, is of great technological importance since it is widely used for producing different ceramics, a wide set of catalysts for numerous industrial chemical processes, adsorbents, coatings, soft abrasives, etc.[1] Owing to technological innovations, new uses are found for alumina each year worldwide. The diversity of applications for alumina can be explained by the surprising range of its physical and chemical properties.[2] This material shows remarkable structural peculiarities and provides a set of different polymorphs. Among them, only α-Al_2O_3 (corundum) is a stable oxide, while γ, δ, η, θ, χ, and κ derivatives are considered to be metastable. They are formed gradually upon the dehydration of various hydroxides and oxyhydroxides[2] and occur in the following transformation sequences:

$$\mathrm{Al(OOH)\ (boehmite/pseudoboehmite)} \Rightarrow \gamma\text{-} \Rightarrow \delta\text{-} \Rightarrow \theta\text{-} \Rightarrow \alpha\text{-}Al_2O_3,$$

$$\mathrm{Al(OH)_3(bayerite)} \Rightarrow \eta\text{-} \Rightarrow \theta\text{-} \Rightarrow \alpha\text{-}Al_2O_3,$$

$$\mathrm{Al(OH)_3(gibbsite)} \Rightarrow \chi\text{-} \Rightarrow \kappa\text{-} \Rightarrow \alpha\text{-}Al_2O_3.$$

It is worth noting that the γ, η, and χ forms are called low-temperature Al_2O_3 phases, whereas δ-, θ-, and κ-Al_2O_3 are regarded as high temperature polymorphs.

There has been much work done on these materials,[2–20] especially in the past decade.[10–17] However, debates over their structure, stoichiometry, and crystal chemistry are still continuing. Wolverton and Hass[12] and Paglia *et al.*[17] provided excellent reviews of the problem, but to make the reader acquainted with situation, we will briefly outline key points.

γ-, δ-, and η-Al_2O_3 are believed to possess a spinel structure with some vacancies distributed over the lattice, thus providing a cation-anion ratio of 2:3. The same ratio in the ideal spinel structure is 3:4. Therefore, the structures of these polymorphs are based not on the ideal but on an imperfect spinel arrangement. The ideal spinel of the $Fd\bar{3}m$ space group is built up of cubic, close-packed arrays of oxygen anions with aluminium cations occupying the tetrahedral (T_d) and octahedral (O_h) interstices related to the 8*a* and 16*d* Wyckoff positions, respectively. Besides, there are additional empty tetrahedra and octahedra in this structure. To give the polymorphs the right Al_2O_3 stoichiometry, it is necessary to introduce some vacancies into the regular lattice but the question of which sites are predominant for them appears to be much debated in the literature. Some authors give preference to tetrahedral interstices,[4,6] whereas other researchers provide some evidence for the existence of vacancies on the octahedral sites[10,16] or consider the vacancy distribution over both types of polyhedra.[5,7] It is also not clear whether the vacancy distribution is ordered or statistical. Moreover, some authors[5,7] report on the possible occupation of nonspinel sites in the structure of γ, δ, and η phases that can lead to another potential misunderstanding. The role of hydrogen and residual hydroxyl groups is also obscure. Several researchers have proposed that the general formula for η- and γ-Al_2O_3 can be written as $Al_2O_3 \times nH_2O$.[3,5,11] Ushakov and Moroz[5] and Soled[18] consider the replacement of some O^{2-} with OH^- ions. De Boer and Houben[3] postulated that γ-Al_2O_3 is crystallized as a hydrogen (proto)spinel of HAl_5O_8 type. Sohlberg *et al.*[11] prefered to give $H_{3m}Al_{2-m}O_3$ notation for γ-Al_2O_3 with a different content of H^+ protons, but other authors,[12] also using first-principles total energy calculations, ruled out this possibility, indicating that the hydrogen-containing form was thermodynamically unstable. The results of other theoretical studies on the possible presence of hydrogen in the bulk of aluminas and their phase transformation mechanisms appear just as contradictory[14–16] though it

seems likely that H^+, OH^- ions, or residual water might play a role in the structural arrangement of these metastable phases and influence the process of phase transition.[11]

Complicating the issue is a pronounced broadening of diffraction peaks in the x-ray diffraction patterns of aluminas, especially of the low-temperature polymorphs. On the one hand, the small size of the coherently scattering domain caused by poorly developed crystallinity in different Al_2O_3 polymorphs is believed to affect this broadening. On the other hand, many researchers agree that the diffuse character of diffraction patterns of transition aluminium oxides reflects a high degree of disorder in their structure. Therefore, the origin of the defect continues to be highly debated in the literature. Lippens and de Boer[19] reported the occurrence of stacking faults in the structure of η-Al_2O_3, but without providing direct evidence. Other authors observed multiple twinning in δ-Al_2O_3,[20] a zigzag arrangement of vacancies[10] and interacting planar defects[13] in the lattice of γ alumina as well as numerous grain boundaries[9] in the same oxide. However, a systematic study of the microstructure of transition forms of Al_2O_3 has not been made yet.

Thus, one can see that there are huge amounts of conflicting experimental data and a lack of consensus in the field of transition aluminas. From our point of view, this situation could not only be related to a varied preparation history of the aluminium oxides, but could also account for the deficiency of diffraction methods for the structural study of the nanocrystalline materials with a high density of defects such as different Al_2O_3 polymorphs. Numerous studies based on the integrated intensities of x-ray and/or neutron powder diffraction peaks or using the Rietveld refinement method have been undertaken to propose a model of cation distribution in the metastable aluminas and to refine their structure. Unfortunately, the results obtained appear to be very conflicting. However, it is obvious that use of a three-dimensional atomic model for the structural refinement of compounds with an imperfect arrangement looks inadequate. Structural disorders, particularly planar defects, result in diffuse scattering effects being exhibited as a specific broadening of the x-ray diffraction peaks or a partial redistribution of their intensity.[21,22] In some special cases, even additional diffuse scattering maxima appear in the spectra.[23] Therefore, before performing the structural refinement of low-temperature Al_2O_3, it is imperative to have a knowledge of the possible effect of the oxide micro(nano)structure on the spectral features of the x-ray diffraction profile. Recently, an approach to the investigation of highly imperfect nanocrystalline compounds based on the simulation of an x-ray powder diffraction pattern and involving a model of one-dimensional (1D)-disordered crystal[23,24] has been developed. As a result, it has become possible to perform x-ray diffraction (XRD) structural analysis of materials with planar defects.[24] Therefore, a new possibility to reexamine the microstructure of different Al_2O_3 forms has emerged now, which would provide a basis for reconciling various sets of seemingly contradictory experimental data available through the literature.

The present paper focuses on the study of the origins of x-ray line broadening observed for low-temperature γ-, η-, and χ-Al_2O_3 polymorphs. For this purpose, x-ray powder diffraction with full profile simulation and systematic transmission electron microscopic analysis of the microstructure of these oxides were performed. A model comprising specifically shaped building nanoblocks of Al_3O_4 composition is proposed and types of their stacking accompanied by the formation of planar defects lying on the {100}, {110}, and {111} planes were revealed. The results reported here provide some understanding of the reasons for line broadening in the x-ray diffraction patterns of the low-temperature aluminas and adequately describe their nanostructure.

II. EXPERIMENT

Samples of low-temperature γ-, η-, and χ-Al_2O_3 were prepared through thermal decomposition of the boehmite (γ-AlOOH), bayerite [$Al(OH)_3$], and hydrargillite [$Al(OH)_3$], respectively. Pseudoboehmite, which is a low-ordered hydroform of boehmite with an $Al_2O_3:H_2O$ molar ratio equal to 1.5, was also used for the synthesis of γ-Al_2O_3. To obtain different alumina derivatives, parent hydroxides were heated in air at 600 °C for 4 h. After calcinations, the samples were cooled down to ambient temperature in the furnace. The γ-oxide synthesized from boehmite will be referred to as γ-Al_2O_3 (B), while that made from pseudoboehmite will be referred to as γ-Al_2O_3 (PB) throughout the text. More details of the preparation procedure can be found elsewhere[25,26]

High resolution transmission electron microscopy (HRTEM) experiments were carried out on a JEM-2010 transmission electron microscope operating at 200 kV and 0.14 nm point resolution. For HRTEM analysis, samples were prepared from suspensions in a methanol slurry. A drop of suspension was placed on the holey-carbon copper grids.

XRD patterns of the samples were collected at room temperature on a D8 Bruker diffractometer equipped with a Cu $K\alpha$ x-ray source and a graphite monochromator with a step size of 0.05°, 2Θ and a count time of 30 s at each step. For the XRD analysis, the samples were grounded in the agate mortar and mounted onto the flat specimen holder.

III. RESULTS

Figure 1 shows XRD powder patterns of low-temperature γ-, η-, and χ-Al_2O_3, exhibiting very diffuse spectra with an extensive reflection overlapping and a profile asymmetry typical for these materials. However, for the moment, let us turn to the results of the HRTEM study to observe the similarities and differences in their nanostructure.

A. High resolution transmission electron microscopy study

Two important points should be noted here. First, it seems very likely that the type of defect characteristic of each polymorph is only a part of the overall defect structure of low-temperature aluminas. However, in each case, this kind of structural imperfection was the only major one observed with the help of a bright-field image and a selected area electron diffraction (SAED) at the resolution limit of the electron microscope in use. Second, SAED patterns of all the samples were indexed within a cubic $Fd\bar{3}m$ space group de-

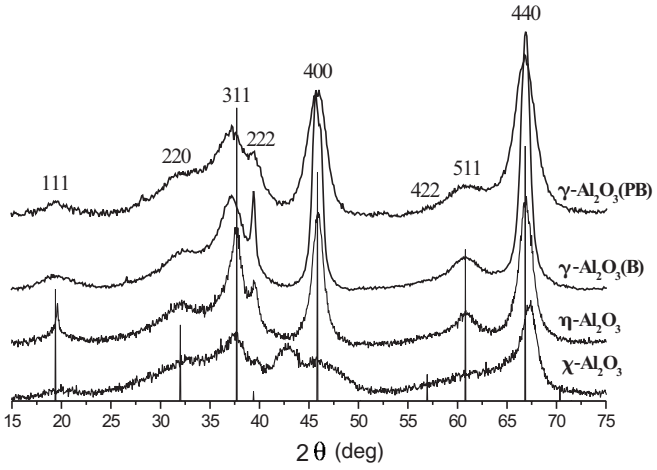

FIG. 1. Experimental x-ray powder diffraction patterns of the low-temperature Al_2O_3 polymorphs. Strip diagram denotes positions of the characteristic spinel reflections with the following indices.

spite the fact that hexagonal notation is traditionally used for the description of a χ-Al_2O_3 structure.

1. γ-Al_2O_3 (PB)

By morphology, this specimen represents aggregates of more than 80 nm in size comprising fine (about 3–5 nm) primary particles randomly oriented to each other in the aggregate, as shown in Fig. 2(a). The SAED pattern taken from the aggregate and given in the inset of Fig. 2(a) exhibits three rings at d_{hkl} values of 0.198, 0.14, and 0.089 nm, corresponding to the 400, 440, and 840 reflections of γ-Al_2O_3. Major defects in the structure of this material are expected to be grain boundaries.

2. γ-Al_2O_3 (B)

In contrast to previous specimen, γ-Al_2O_3 particles have a plateletlike morphology with sizes of 100 and 60 nm along and across the platelet, respectively. The thickness of this flat particle does not exceed 15 nm. SAED patterns frequently observed in this specimen correspond to the [110] zone axis and Fig. 2(b) shows the HRTEM image along with a diffraction pattern of an γ-alumina platelet oriented into the $\langle 110 \rangle$ pole. Point reflections visible in SAED pattern reflect the single crystalline character of the platelet structure. The most significant observation of this material concerns the presence of specific defects in the characteristic crystallographic morphology marked by arrows in the micrograph. They look like loops, having an almost regular hexagonal shape, and are bounded by {111} and {100} type crystal planes. The observed loops cannot not be considered as voids or pores since a tilt of the oxide microcrystal in the microscope of several degrees leads to their disappearance from the image, thus indicating the dislocation nature of these defects.[27,28] Similar structures have been reported by Tsybulya *et al.* for $MgAl_2O_4$ prepared by calcination of Mg-impregnated boehmite[29] and Mn-doped Al_2O_3.[30] It was found that the formation of such closed loops may occur only if the partial dislocations lying on the (110) and (111) planes appear simultaneously in the oxide material and generate planar defects associated with ordered vacancies located on the octahedral sites which are usually occupied in a regular spinel. Therefore, following an early observations,[10,13] we suggested that loops generated in the structure of γ-alumina are due to the process of coalescence of cation vacancies.

The SAED pattern taken along the [110] zone axis shows different reflection shapes as well. While the 440 reflection has a relatively high intensity and a symmetrical shape, the 220 reflection, which is low in intensity, is streaked in the [001] direction that indicates some disorder in stacking between the (001) planes.

3. η-Al_2O_3

Aggregates shaped like a sand clock and composed of numerous platelets with sizes ranging from 50 to 600 nm have been found to be the predominant morphological type in this specimen. According to the SAED pattern shown in the inset of Fig. 2(c), most developed plane of the individual platelet is of the (111) type. This figure also represents the HRTEM image of the platelet in plane view along with the side view inserted into the upper right corner of the micrograph. The individual platelet consists of domains of 4 nm in size terminated by planes of the {110} type with an angle of 120° in between that can be clearly seen near the platelet edge in this image. The packing of the nanosized domains in the (111) plane appears to be almost coherent since the SAED pattern taken from the crystal exhibits a regular spotlike character. At the same time, the shape of the first- and second-order reflections in this pattern looks different. While the $4\bar{4}0$ reflection is sharp and pointlike, the reflection with a $2\bar{2}0$ indices looks homogeneously broadened. This may be due to the possible presence of a structural disorder in the direction perpendicular to the (111) developed face of the oxide particle, i.e., along the [110]. In this case, the faults would be seen "edge-on" and appear as a line in the image that is consistent with well defined contrast of the boundaries between nanodomains clearly visible in the HRTEM micrograph. The structure, viewed in the lateral projection of the platelet along the $[1\bar{1}\bar{1}]$ zone axis, exhibits some dislocations which arise upon stacking the (111) planes, as arrowed in Fig. 2(c). It should be noted that some faults may appear as well if isolated plateletlike crystals are joined into big aggregates with an increased thickness from 20 to 400 nm.

4. χ-Al_2O_3

Oxide particles in this specimen are crystallized in the shape of thin isolated platelets without any aggregation. The sample has a broad size distribution and particle sizes are in a range of 10–100 nm. Likewise, η-Al_2O_3, the most developed plane of the platelet, was found to be the (111) according to the SAED pattern shown in Fig. 2(d). Again, each plateletlike crystal consists of several domains. Their packing inside the crystal body seems to proceed almost coherently since the electron diffraction pattern shows a spotlike character. However, in contrast to η alumina, this pattern

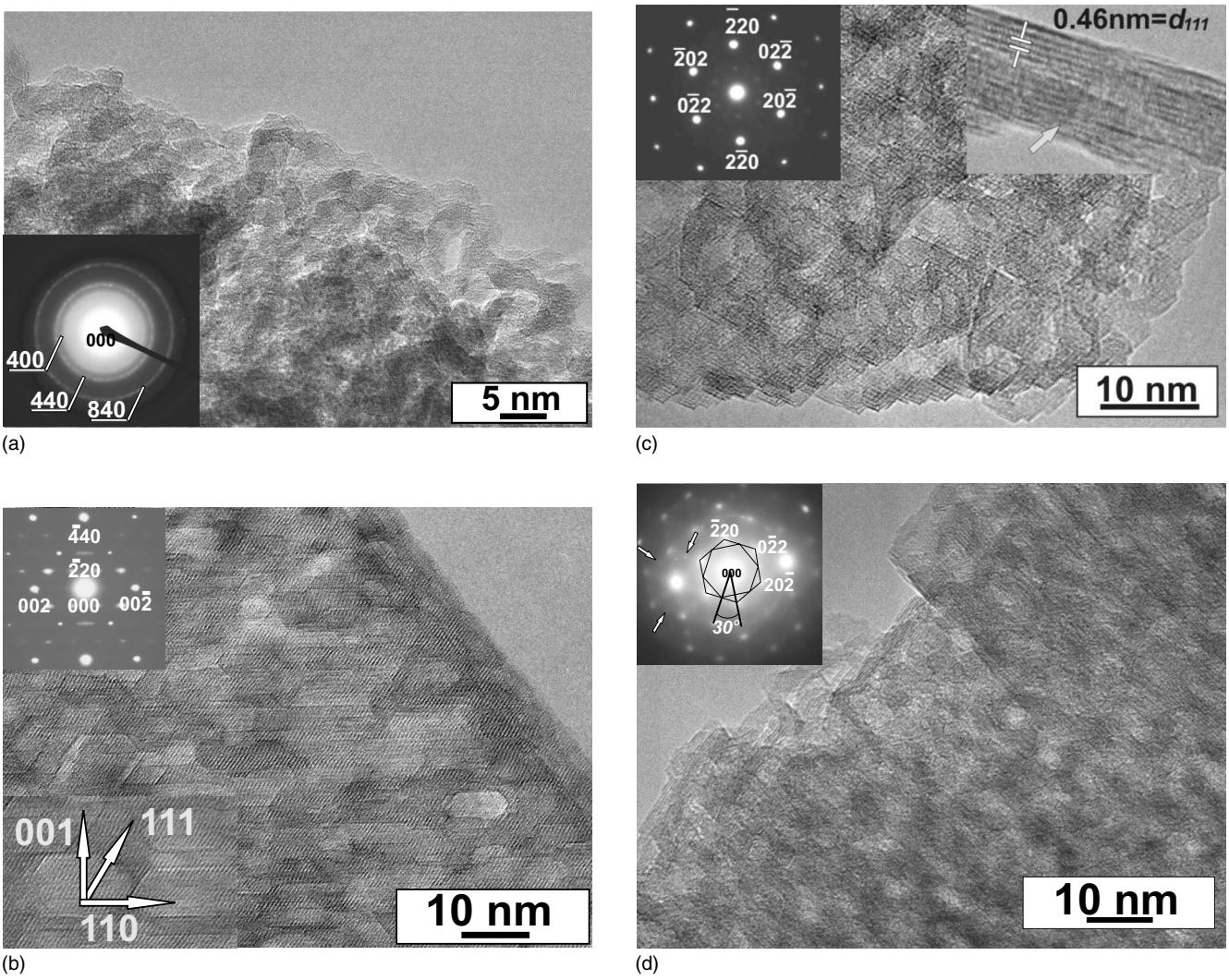

FIG. 2. Structural characterization of the low-temperature alumina polymorphs by HRTEM. (a) γ-Al_2O_3 (PB) image with the SAED pattern. (b) γ-Al_2O_3 (B). Insets show the SAED pattern and the magnified image of the hexagonally shaped defect (left-hand bottom). (c) η-Al_2O_3 image with the SAED pattern. Right-hand inset shows the lateral projection of the same particle with a dislocation (arrowed). (d) HRTEM image of the χ-Al_2O_3 nanoparticle and corresponding SAED pattern (top) with an additional reflections (arrowed) uncharacteristic of the spinel structure. Inset shows also a possible rotation shift between identical diffraction motives with the designation of the rotational angle.

looks more complicated. Although indexed as coming from the [111] zone axis, it exhibits additional, very weak but recognisable spots located between the main reflections and marked by arrows in the inset of Fig. 2(d). Such a complicated pattern may be attributed to the superposition of two identical diffraction motives rotating around each other at 30°, as schematically drawn in the same figure. The structural mechanism that best satisfies the observed diffraction behavior seems to be twinning. We suggested that the crystalline domain is moving around a sixfold axis at 30° inside the (111) plane, thus providing a kind of twin-related fragment with respect to the underlying oxide layer, and a rotational shift between nanocrystalline blocks dominates in the structure of this oxide.

Summarizing the results of HRTEM analysis, we can conclude that the low-temperature alumina derivatives possess numerous defects which are specific for each polymorph. Now, let us look at how these defects may influence the broadening of the diffraction peaks in the XRD patterns of these materials.

B. X-ray diffraction analysis and simulation of the diffraction profile

Comparing all XRD patterns represented in Fig. 1, one can see distinct differences in

(a) the formation of a very peculiar shape of the 111 reflection with a broadened base and sharp top only for the η phase,

(b) a shape resemblance of the 220 reflection for γ, η, and even χ polymorphs and an anomalous broadening of this peak in comparison with the 440 reflection, and

(c) a shift of the 311 reflection to a lower angle exclusively for both γ-alumina specimens compared with calcu-

lated and experimental positions of the same reflection for the η and χ forms.

Here, it should also be noted that a light splitting of the 400 reflection for boehmite-derived γ-Al_2O_3 indicates, according to previously published results,[7] a tetragonal distortion of the spinel structure.

How can this x-ray line-shape information be bounded with faulting on different planes observed by HRTEM? A simulation of XRD patterns by using an imperfect spinel with specific planar defects as a model could provide an answer. Details of the computational approach for full profile simulation of XRD powder patterns are described elsewhere.[24,31] Here, we will only briefly outline basic principles.

Simulations are performed with the model of the 1D disordered crystal described as a statistical sequence of a finite number of different two-dimensional (2D) periodic layers. The calculation program[31] is based on the Kokinoki-Komura matrix algorithm.[32] The x-ray intensity distribution for the sequence of infinite layers is given by

$$i_{hk}(l) = \frac{1}{\Omega\sigma}\left\{ \mathrm{Tr}\,\mathbf{FW} + 2\,\mathrm{Re}\sum_{n}^{N-1}\frac{N-n}{N}\mathrm{Tr}\,\mathbf{FWQ}^{n}\right\},$$

where h and k are integer Millers indices, l is a continuous variable, **W**, **F**, and **Q** are square matrices determined by the layer structural factors and some probability parameters responsible for the layer appearance in the stack, and Ω and σ are some normalization factors.

Assuming that each 2D layer has a regular arrangement, a stacking fault or other planar defect can be simulated simply by shifting or rotating these layers with respect to each other, and alternatively, by alternating their sequence in the stack. A mathematical approach to the problem of the calculation of the scattering intensity from such a fault is reduced to the calculation of probabilities of the appearance of any layer in a given position inside the layer stack. Additional probability parameters are introduced as factors showing how 2D layers alternate and/or displace each other in the stack. The probability process comprises a Markov chain of order m ($m \geqslant 1$) if the probability of a new state depends only on the m number of the former states preceding the new one. As a result, randomly distributed or correlated planar defects may be specified, and the total distribution of the scattering intensity from imperfect structure can be calculated with corrections for some instrumental parameters such as line broadening, adsorption, and background. The effects of the finite size and the shape of layers on the diffraction profile are also taken into account. The calculation involved reads

$$i_{hk}(\mathbf{s}) = i_{hk}(l)G(\varepsilon_h, \varepsilon_k),$$

where **s** is a reciprocal space vector and $G(\varepsilon_h, \varepsilon_k)$ depends on the size and shape of the layer in the (xy) plane. To determine the quality of the fit between theoretical and experimental profiles of the XRD pattern, a visual inspection and the numerical R_p factor are used.

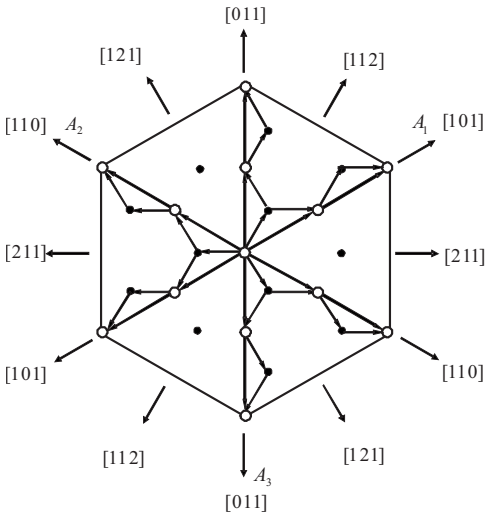

FIG. 3. Scheme of the mechanisms of the dislocation splitting inside the (111) plane of the spinel structure, based on Fadeeva *et al.* (Ref. 33).

The choice of the model used for our simulations begins with the spinel structure described in the framework of the cubic unit cell with $\boldsymbol{a}$ lattice parameters. In generalized crystalline chemistry analysis, a light tetragonal distortion of this lattice can be neglected. To perform the simulation of the diffraction pattern from the spinel structure with defects lying on the specified plane system, it is imperative to choose a new basis with the $\boldsymbol{c}'$ axis perpendicular to the analyzed plane system. The configuration of the stacking fault strongly affects the type of the single or several layers which are the building units for the simulation. In a separate series of computations, we studied the effects of different planar defects on the spinel diffraction patterns. However, we will not now discuss a huge massive of calculation results, but only those which help to explain some peculiarities of the diffraction profiles of low-temperature alumina polymorphs.

1. Faulting on the {111}: Shape of the (111) reflection

The 111 peak in the XRD pattern of η oxide comprises the superposition of two components, one sharp and one broad, while a similar peak in the γ(B) polymorph looks very diffuse. However, this is not due to the size effect since the 222 peak is the narrowest and the calculation of the particle size obtained with half-width at half maximum (HWHM) of this reflection provides a value equal to 12 nm. For η oxide, the particle size calculated with HWHM of the sharp component of the 111 peak was about 35 nm, very close to the dimension of platelet in the lateral projection that has been directly measured in the HRTEM micrograph. The HRTEM also confirmed that faulting occurs on one of the four plane systems of the {111} type in the structure of the η polymorph. Therefore, one (111) plane system appears as specified, compared with the remaining three {111} planes.

Usually, stacking fault defects are bounded by partial dislocations. Figure 3 shows the scheme of the mechanism of the dislocation splitting in the spinel structure as it was described by Fadeeva *et al.*[33] According to this scheme, a

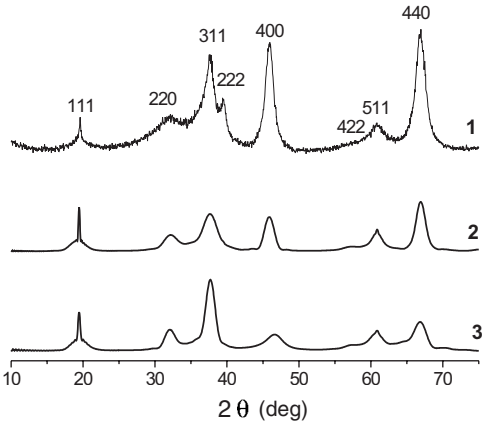

FIG. 4. Experimental (1) x-ray diffraction pattern of the η-Al_2O_3 and theoretical profiles calculated for a spinel with defects lying on the plane system of the {111} type and bounded by (2) half and (3) quarter dislocations at the defect density equal to 20%. Cylindrical shape of the particle with 6 nm diameter and 35 nm height was used for the calculations. These values were determined with HWHM of 440 reflection and the narrow component of the 111 peak, respectively.

bounding half dislocation lying along the ⟨110⟩ direction does not disturb the oxygen sublattice in this structure. Vice versa, a quarter dislocation in the ⟨112⟩ has a pronounced effect on the coherency of the oxygen closed packing.[33–35] Theoretical patterns calculated with quarter and half dislocations are given in Fig. 4. As one can see from this figure, both models lead to the complicated shape of the 111 reflection owing to the superposition of two sharp, unaffected components from scattering over the single fault-included {111} plane system and six broad components from scattering over the remaining three undisturbed plane systems of a similar type. However, in the case of the model with quarter dislocations, a very broad 400 reflection appears in the calculated XRD pattern, in contrast to a relatively narrow peak in the experiment. Therefore, we concluded that stacking faults appearing on the (111) plane in the structure of η-Al_2O_3 are bounded by half dislocations.

Compared to η-Al_2O_3, the shape of the 111 reflection in γ-Al_2O_3 (B) strongly differs, as shown in Fig. 1. The specific shape of this substantially broadened reflection without a resolved narrow component originates from the presence of faulting not on the single but on the two plane systems of the {111} type. It is obvious that the sharp component of the 111 peak caused by individual stacking defects lying on one plane of a given family, e.g., (111), will transform into a broadened line if the interconnecting faults appear on different planes such as the $(11\bar{1})$ and $(\bar{1}11)$. It became evident that the 1D model used as the basis in our structural approach inevitably introduces some limitations.[36] It is possible to calculate full diffraction profiles for a structure with faults lying only on a *single plane system*, but in the case of interacting defects that appear simultaneously on *several plane systems*, such a calculation fails. To overcome this limitation, the theoretical shape of the 111 reflection rather than a whole diffraction profile was calculated for both polymorphs. Experimental and theoretical shapes are given in Figs. 5(a) and

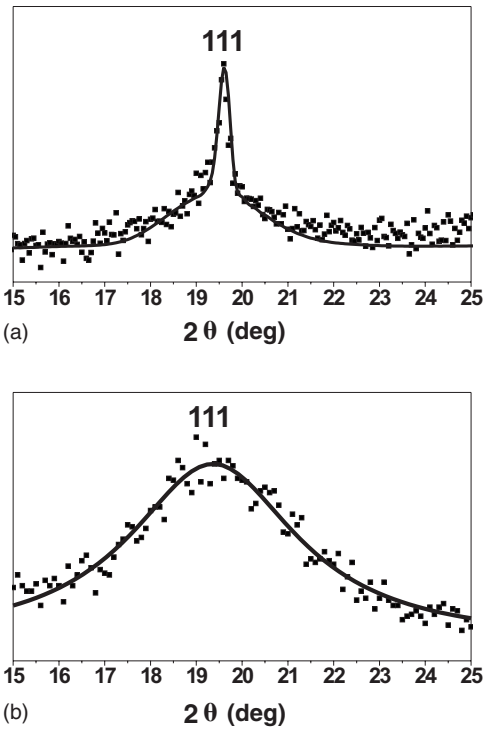

FIG. 5. Theoretical (bold line) shapes of the 111 reflection calculated for a spinel with (a) defects lying on the single plane of the {111} family and bounded by the half-dislocation and with (b) intersecting defects on the $(1\bar{1}1)$ and $(\bar{1}11)$ planes bounded by the half-dislocations at the dislocation density equal to 20%. Dots denote experimental shapes of the same reflection for (a) η-Al_2O_3 and (b) γ-Al_2O_3 (B).

5(b). For this single reflection, computations accounted for the superposition of eight components, each being a convolution of the broadening function that arises owing to defects on the $(11\bar{1})$ and $(\bar{1}11)$ planes. As one can see in Fig. 5, a good fitting between theoretical and experimental shapes of 111 reflections for η-Al_2O_3 and γ-Al_2O_3 (B) was obtained that confirms the proposed defect configuration.

2. Faulting on the {110} and {100}: Shape of the 220 reflection and shift of the 311 peak

Introducing faulting on the {111} enabled us to explain why the 111 reflection undergoes broadening but could not provide an explanation of the origin of specific shapes of other reflections in the experimental XRD patterns. First of all, it concerns the shape of the 220 peak. If we only take defects lying on the {111} into account, this would lead to misleading results unless the presence of faulting on the others, the {110} and {100} planes, is not considered. For both cases, all possible types of faults were outlined earlier[34] and gliding systems in the spinel that do not disturb the anion close packing but affect the cation sublattice are summarized in Table I. All theoretical results shown below were obtained using the listed configurations of defects.

For the simulations, the particles had the shape of a regular cylinder with a diameters and heights ranging from 5 to 50 nm. The concentration of the stacking defects

TABLE I. Gliding systems in the {100} и {110} planes that preserve ordering of the oxygen sublattice but introduce some distortions into the cation sublattice in the spinel structure.

	Plane	Gliding direction	Vector
1	{100}	⟨100⟩	$1/2\mathbf{a}_1$
2	{100}	⟨110⟩	$1/4\mathbf{a}_1+1/4\mathbf{a}_2$
3	{110}	⟨110⟩	$1/4\mathbf{a}_1+1/4\mathbf{a}_2$
4	{110}	⟨100⟩	$1/2\mathbf{a}_1$

changed from 10% to 30%. Two main conclusions could be derived from the theoretical results shown in Fig. 6. First, any defect mentioned in Table I, similar to faulting on the {111} associated with half dislocations, does not broaden the 400 and 440 reflections at low defect concentrations as evident from Fig. 6(a). Therefore, these peaks are useful for the determination of the particle size in spinels if the stacking fault defects which influence the closed packing of oxygen sublattice do not appear in the spinel structure. Second, all defects listed in Table I are not responsible to the shift of the 311 peak. Additionally, they do not smear all the components of the 220 reflection. It is interesting to note that a line shape of theoretical patterns calculated with a small particle size and 10% density of planar defects may be formally attributed to the peak-broadening effect of the nanosized crystals [see Fig. 6(b)]. However, the theoretical profile changes drastically when the defect density rises above 10% since additional peaks of diffuse scattering, originating from the accumulating phase shift of the scattering wave across numerous faults, appear in the vicinity of some Bragg reflections, as indicated with arrows in Fig. 6(c). As the particle size decreases, the stronger overlapping between Bragg reflections and additional maxima can be seen in the theoretical profiles [Fig. 6(d)]. Hence, we note that experimental diffraction peaks observed in the XRD patterns of low temperature polymorphs and usually attributed to the broadened "111," "220," "311," and "511" spinel reflections actually comprise the superposition of Bragg maxima with additional peaks of diffuse scattering if the regular spinel arrangement transforms into a strongly distorted—situation typical for the imperfect alumina derivatives.

The computation also provided the evidence that the presence of stacking faults lying on the {100} with ⟨100⟩ displacement vectors gives rise to the formation of an additional maximum of diffuse scattering at the angle region of ~36°, 2Θ. With a small (less than 10 nm) particle size and a low (around 10%) density of these defects, the 311 Bragg reflection strongly overlaps this additional peak and the superimposed peak shifts to the lower angle region of the theoretical diffraction profile. This effect appears to be more pronounced with the increase of the defect density up to 30%. As can be seen in Fig. 7(a), curve 2, the shift of the gravity center of the 311 resulting peak is as strong as 0.3°, 2Θ compared to the position of the same reflection in the experimental XRD pattern of γ-Al_2O_3.

Earlier, as reported by Zhou and Snyder,[7] the displacement of the 311 reflection in γ-Al_2O_3 to a lower angle region was accounted for by a pronounced tetragonal distortion of the structure of this material. Indeed, splitting the 400 reflection can be observed in the experimental XRD pattern of the γ-Al_2O_3 specimen that may initially be assigned to the lattice distortion. The lattice parameters calculated with accounting for this splitting appear as follows: $a=0.7941$ and $c=0.7876$ nm. However, in contrast to the experiment, the shift of the 311 peak, which might possibly occur due to such a splitting, is practically unrecognizable in the theoretical diffraction pattern, as shown in Fig. 7(b). The profile with narrow peaks plotted in the same figure denotes the calculated XRD pattern of the regular spinel structure without any defect. Therefore, our computation indicates that the faulting on the {100} plane is the origin of the observed diffraction effect.

Additional computations revealed that anomalous broadening of the 220 reflection caused by the faulting of the {110}⟨110⟩ type is generally attributed to two factors: (i) the inherent smearing of all components of this peak and (ii) the appearance of an additional diffuse scattering with the maximum located at ~28°, 2Θ, as can be seen in Fig. 6(c), curve 3. However, if a planar defect lies perpendicular to the single specified direction from the ⟨110⟩ family, some components of the 220 peak do not undergo broadening and only the particle size affects the HWHM of this reflection, as illustrated in Fig. 8(a). By optimizing the particle size and density of a planar defect of this type, it is possible to get a reasonable fitting between theoretical and experimental profiles of the 220 peak for γ(PB) alumina with their fine particles [Fig. 8(b)]. Alternatively, for γ-Al_2O_3(B) as well as for η-Al_2O_3, such a comparison fails as is evident from Fig. 8(a). Obviously, the reason is similar to the case of the broadening of the 111 peak: we must account for several interacting planar defects lying on different plane systems that are consistent with the HRTEM evidence on the various kinds of faults lying on several plane families in the structure of alumina polymorphs. How can the mutual presence of these defects affect the shape of the 220 reflection? To address this problem, additional simulations have been performed.

The results are summarized in Table II. They show that defects of the {110}⟨110⟩ type presented simultaneously on three symmetrically identical (110), (101), and (011) planes affect all components of the 220 reflection and make them smear. Moreover, computations definitely confirm that each component of the 220 peak is broadened by two defect systems, i.e., faults on the (101) and (011) with displacement vectors parallel to the $[10\bar{1}]$ and $[01\bar{1}]$ directions, respectively. These defect configurations influence the width of the 220/002 component. Such a situation is characteristic of η-Al_2O_3 particles with their well developed faces belonging to the {111} family. Concerning γ—Al_2O_3 (B), we suggested that the mutual occurrence of the defect on the (110) and two different faults on the $(11\bar{1})$ and $(1\bar{1}1)$ planes causes broadening of all components of the 220 peak.

3. Peculiarities of x-ray powder diffraction pattern of χ-Al_2O_3

Regarding faults, it seems likely that χ-Al_2O_3 is no exception. First of all, for this polymorph, like other low-

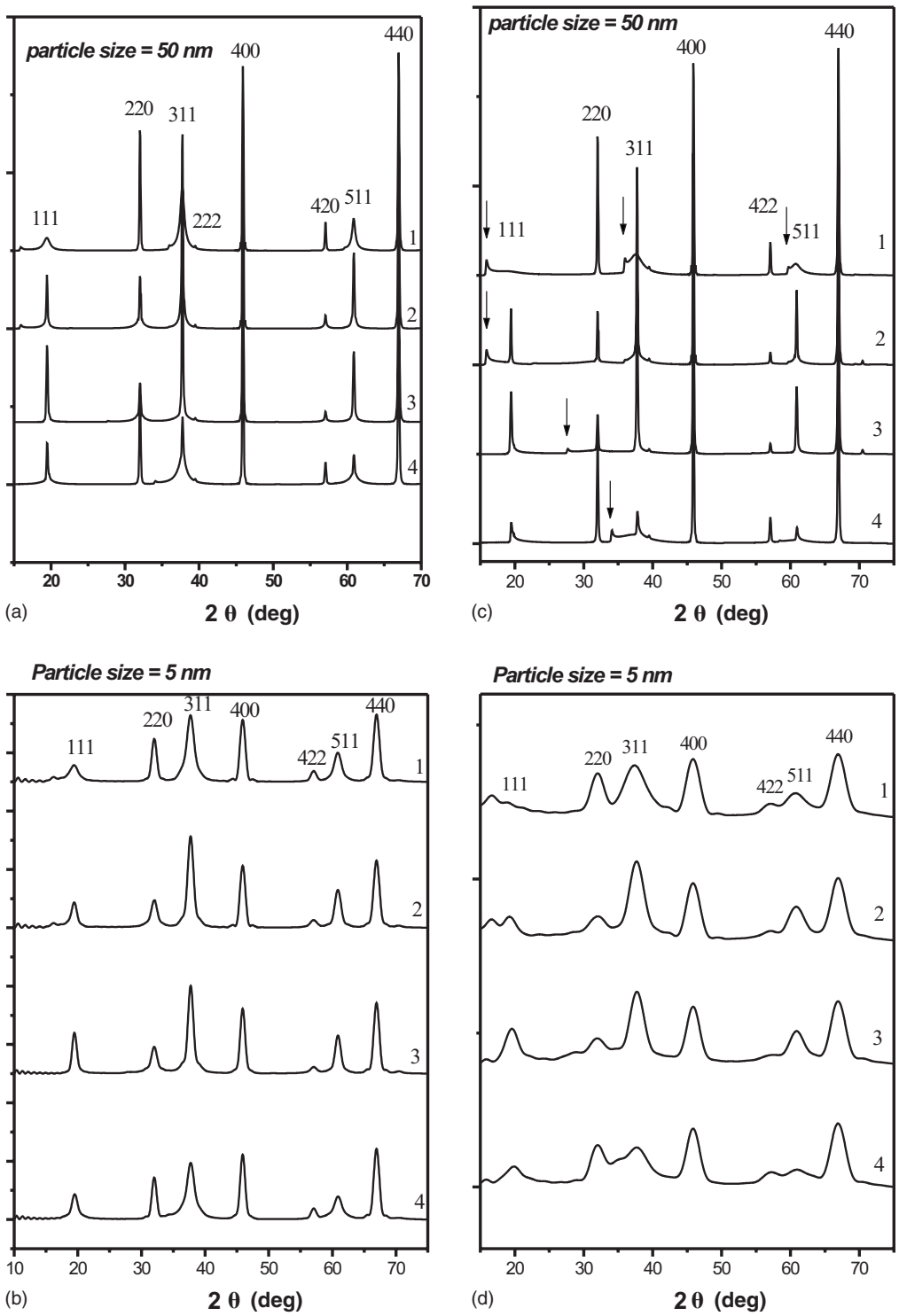

FIG. 6. Theoretical profiles calculated for the imperfect spinel. Curve numbers denote the defect configurations listed in Table I. Particle size differs from 50 to 5 nm, while the defect density increases from [(a) and (b)] 10% to [(c) and (d)] 30%.

temperature forms of alumina, the anomalously broadened 220 reflection is clearly visible in the XRD pattern. As it was shown for η- and γ-Al_2O_3, the simultaneous presence of several interacting systems of planar defects gives rise to this kind of peak broadening. At the same time, contrary to γ-Al_2O_3, the shift of the 311 reflection was not observed in the XRD spectrum. According to the HRTEM analysis, the most developed plane of the χ-Al_2O_3 microcrystal is the (111), similar to η-Al_2O_3. Therefore, this form looks closer to the η derivative than to the γ oxide. The distinctive feature of χ alumina is associated with an additional peak that appears exclusively at 42.8°, 2Θ in the experimental XRD pattern of this material. Many authors[2,3,9] have related this characteristic diffraction effect to the faulting, which is so

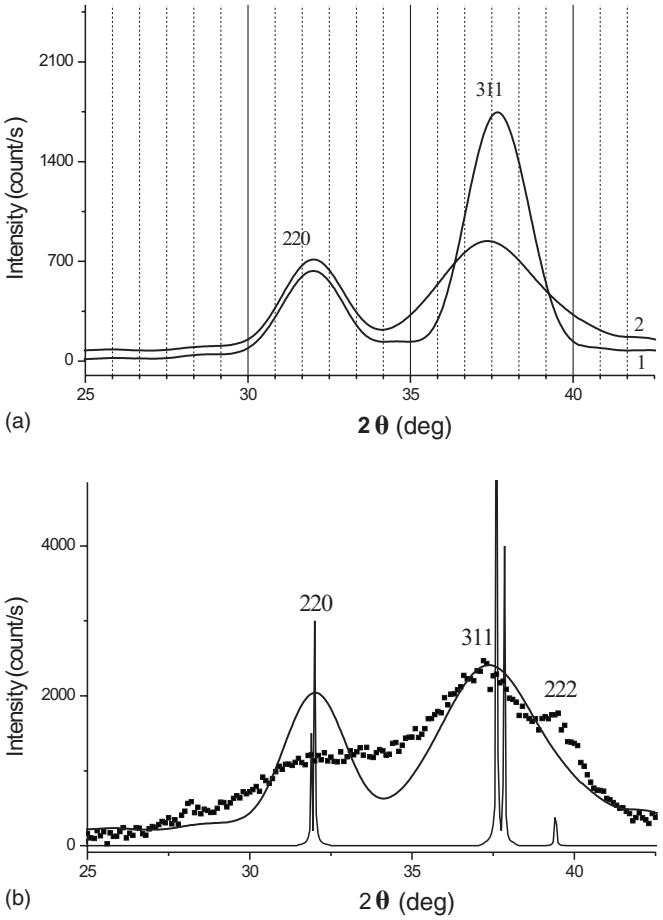

FIG. 7. Shift of the 311 diffraction peak as a result of the presence of stacking fault defects on (100) plane with the $1/2a$ [010] gliding vector. (a) Parts of the theoretical profile calculated for a spinel without any defect (1) and at the increased defect density of 30% (2). (b) Comparison between the theoretical profile calculated for a spinel with defects of similar type at 30%-defect density (bold line) and experimental (dots) profile of the γ-Al_2O_3 (PB). The theoretical profile with narrow peaks is related to the spinel structure with a tetragonal distortion (a=0.7941 and c=0.7876 nm).

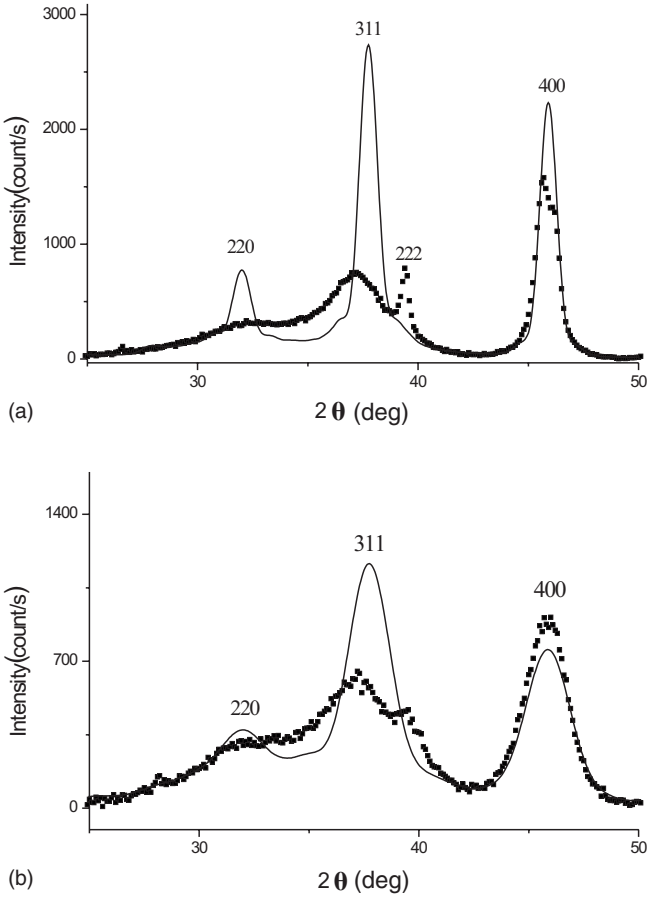

FIG. 8. Theoretical (bold line) shapes of the 220 reflection calculated for a spinel with defects on the {110} plane systems in the case of 20% defect density and particle size equal to (a) 10 and (b) 4 nm. Dots denote experimental shapes of the similar reflection for (a) γ-Al_2O_3 (B) and (b) γ-Al_2O_3 (PB).

strong that the cubic closed packing of the anion sublattice transforms into hexagonal one. However, we could not agree with this hypothesis since, if accepted, the close resemblance between XRD patterns of all low-temperature polymorphs would inevitably be ignored. Moreover, a spinel model could not be used for the description of their structure.

The observed diffraction effect may have another origin since the HRTEM provides some evidence for the possible twinning in the structure of χ-Al_2O_3. Therefore, it was particularly interesting to determine whether spinel-comprising twin-related domains lying on the (111) plane may be consistent with the appearance of an additional diffraction peak in the XRD pattern of this polymorph. For our simulation, we purposely used a model of twinned nanodomains statistically rotated at the angle of 30° with respect to each other as was proposed on the basis of HRTEM observations. In the spinel structure, such a rotational shift results in the change of the oxygen stacking sequence of the $ABCABCABC\cdots$ type for $ABC\mathbf{AB}ABC\cdots$. The computations showed a relatively good agreement with experiment. As can be seen in Fig. 9, the theoretical XRD pattern exhibits a whole set of spinel reflections plus a single additional maximum caused by diffusion scattering over multiple faults. In this figure, an asterisk marks this diffraction feature. Obviously, the calculation results have not been optimized because we were unable to take the twins on the (111) and faults arising upon domains stacking along (110) lateral faces into account simultaneously. Nevertheless, the calculated profile looks similar to the experimental diffraction pattern of this polymorph. This strongly supports a spinel concept for the description of the χ-Al_2O_3 structure.

IV. DISCUSSION

A combined experimental and computational approach used in this study allowed us to describe some peculiarities of XRD patterns of different low temperature alumina derivatives. This method provided possibilities for the discrimination of diffraction effects caused by different types of faulting. Though the model of 1D disordered crystal could not account for numerous cases of lattice distortions, particularly the interacting defects in the structure of low-

TABLE II. Effect of the stacking fault configuration on the broadening of components of the 220 reflection. +: Component is broadened in the case of this defect configuration and −: Component is not broadened in the case of this defect configuration.

	Reflections in cubic/orthorombic axes					
Defect type	220/002	202/211	022/2$\bar{1}$1	2$\bar{2}$0/020	20$\bar{2}$/$\bar{2}$11	0$\bar{2}$2/21$\bar{1}$
(110)[1$\bar{1}$0]	−	+	+	−	+	+
(110)[10$\bar{1}$]	+	−	+	+	−	+
(011)[01$\bar{1}$]	+	+	−	+	+	−
	Reflections in cubic/hexagonal axes					
	220/0$\bar{1}$4	202/$\bar{1}$14	022/104	2$\bar{2}$0/$\bar{2}$10	20$\bar{2}$/110	02$\bar{2}$/$\bar{1}$20
(1$\bar{1}$1)[$\bar{1}$10]	+	−	+	−	+	−
($\bar{1}$11)[1$\bar{1}$0]	−	+	−	+	−	+

temperature Al_2O_3, the principal conclusion of this study is that we were able to identify major types of the structure faulting in these materials and to relate them to the specific shapes of diffraction profiles.

The computation of the full diffraction profile involved a model of regular spinel and unambiguously showed that the presence of the stacking faults of $a/2\langle 100\rangle\{100\}$ type result in the shift of the 311 reflection, while the mutual appearance of several intersecting faults lying on the {111} and/or {110} planes causes a broadening of all components of the 220 diffraction peak. The complicated shape of the 111 reflection, with a broad base and a sharp top, seems to be associated with the individual, noninteracting defects lying on one of four plane systems of the {111} type.

During this study, it also became evident that we should take into account the orientation relationships between most developed faces of the oxide particles, planes, and directions of faulting. Thus, particles of γ alumina prepared from pseudoboehmite do not possess a preferable faces; therefore, the types of defects could not be specified in this specimen.

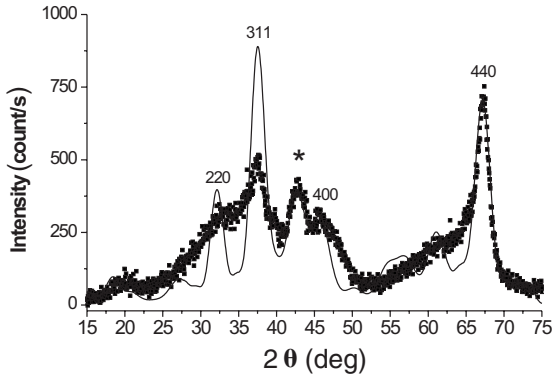

FIG. 9. Experimental XRD pattern of the χ-Al_2O_3 (dots) and theoretical profile (bold line) calculated with the model of twins on the (111) with a rotational shift of 30° at 30% density of the twin boundaries in the spinel structure. Additional peak of the diffuse scattering that appear due to the twinning is marked with an asterisk.

Faulting may occur on any plane belonging to the definite plane family. Alternatively, defects in γ-Al_2O_3 (B) and faults in η-Al_2O_3 are strongly specified owing to the well-developed (110) and (111) faces of their particles. Regarding diffraction peculiarities, χ-Al_2O_3 shows a similarity with η-Al_2O_3 but, in contrast to the latter, has twins in the structure that introduce distortions into the oxygen sublattice. Accordingly, Table III shows indices of those plane families where the faulting appears.

An additional, important conclusion concerns the novel information about the nanostructural architecture of the low-temperature Al_2O_3. We can get calculation results by formulating the structural unit common to all low-temperature aluminas. Despite some variation in the microstructure of these materials, it seems likely that units, which are similar in composition and crystal arrangement but different in shape, could be served as building blocks for the structural description of the whole row of the alumina derivatives. Interacting planar defects may act as boundaries which enclose some minimal volumes (domains) with an internal, regular structure of the spinel type. Plateletlike nanosized domains bounded by different faces and shown in Fig. 10(I) can be considered to be such primary blocks. Variants "a" and "b"

TABLE III. Main types of the stacking fault defects in the low-temperature alumina polymorphs.

Gliding system	γ-Al_2O_3 (B)	γ-Al_2O_3 (PB)	η-Al_2O_3	χ-Al_2O_3
{111}⟨110⟩	(1$\bar{1}$1)[$\bar{1}$10]	{111}⟨110⟩	(111)[$\bar{1}$10]	Twins on (111) plane
{111}⟨110⟩	($\bar{1}$11)[1$\bar{1}$0]			
{100}⟨100⟩	(001)[100]	{100}⟩100⟩		
{110}⟨110>	(110)[1$\bar{1}$0]	{110}⟨110⟩	($\bar{1}$10)[110]	($\bar{1}$10)[001]
{110}⟨100⟩	(110)[001]	{110}⟨001⟩	($\bar{1}$10)[001]	($\bar{1}$10)[001]
			(10$\bar{1}$)[101]	(10$\bar{1}$)[101]
			(10$\bar{1}$)[010]	(10$\bar{1}$)[010]

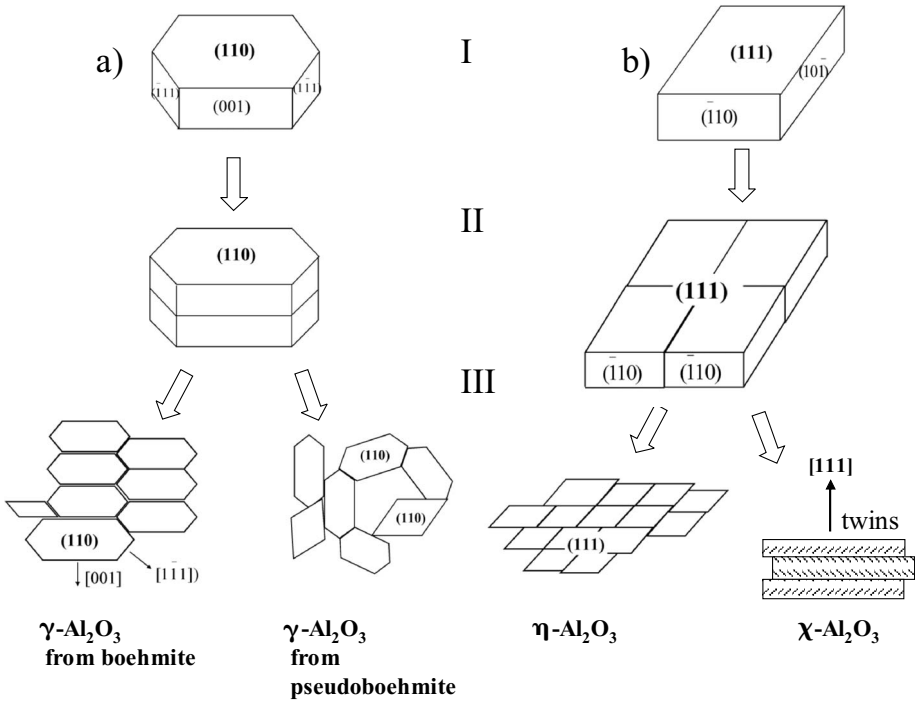

FIG. 10. The structural hierarchy in the alumina polymorphs showing (I) two basic shapes of the primary nanodomains, (II) different ways of their stacking along the (110) plane, and (III) the resulting microstructure.

are not identical since, in both cases, platelets have faces of the {110} and {111} types, however, only "a" particles have also faces of {100} type. Thus, the γ-Al_2O_3 (B) domains of the a type could be joined on several planes, namely, (001), $(\bar{1}11)$, $(1\bar{1}1)$, and (110). According to HRTEM, most developed face of the γ-oxide particle was found to be (110). Variant b suits both η- and χ-Al_2O_3 because their crystals have the most developed plane of the (111) type.

Important to this concept is a suggestion that domains should be arranged into an extended oxide structure through the generation of planar defects specific for each polymorph. This process is schematically drawn in Figs. 10(II) and 10(III). If one a platelet is gliding with respect to the other in the $\langle 110\rangle$ direction, stacking faults of the $\{110\}\langle 110\rangle$ type are produced leaving the oxygen cubic packing undisturbed but inducing some distortions into the cation sublattice of γ-Al_2O_3. η-Al_2O_3 particles with (111) developed planes can be built up by stacking b-type blocks along the $(\bar{1}10)$ and $(10\bar{1})$ faces. This leads to the generation of stacking faults bounded by half dislocations. A similar shape of the nanoblocks is expected for χ-Al_2O_3, but the structure growth proceeds here by twinning on the (111) plane followed by the generation of stacking fault defects in the anion sublattice.

Present evidence allows us to propose a generalized structural model based on the concept of building blocks for all low-temperature alumina polymorphs. In this approach, the microstructures of different transition forms of Al_2O_3 are considered to consist of sets of the nanosized domains, each with the shape specific for a definite polymorph, and each with the potential to interact with neighboring domains through a generation of defects, thus forming the continuous oxide structure. For the explanation of the reasons for broadening of x-ray diffraction peaks in these materials, we purposely used a model comprising the regular Al_3O_4 (spinel) inside the building block. Defects appeared in the process of assembling these blocks into an extended crystalline structure may yield specific ratios of vacancies necessary for maintaining the Al_2O_3 stoichiometry. HRTEM observations definitely support this suggestion since the formation of vacancy loops bounded by half-dislocations was found in the γ-Al_2O_3 specimen under study, as shown in Fig. 2(b). The presence of the vacancy chains in the nonstoichiometric Mg-Al and Mn-Al spinels has been also reported in our previous papers.[29,30]

Now, we will attempt to interpret how a planar defect formed at the contact zone between two domains with an Al_3O_4 composition can affect the charge balance and nonstoichiometry of the resulting oxide structure. The faulting on the {110}, which is observed rather frequently in low-temperature Al_2O_3, will be considered below as one of the examples. Other planar faulting, in particular, models of the stacking fault defects on the {111}, resulted in the formation of vacancy walls in the spinel one can find elsewhere.[24,29]

As was considered above, the stacking of two crystalline blocks on the {110} planes may proceed through their mutual shift on the half-translation vector along the $\langle 100\rangle$ or $\langle 110\rangle$ directions. With the crystalline chemistry approach, this process can be described as follows. In the [110] direction, the ideal spinel structure consists of the sequence of flat atomic sheets of the $|ABO_2|BO_2|ABO_2|BO_2|ABO_2|\cdots$ type where A and B represent cations in the tetrahedral and octahedral environments coordinated by oxygen atoms, respectively. ABO_2 layers appear to be linked through bridging corner-shared BO_2 in such a way that edge-shared octahedra form infinite chains along the [110] direction. The projection of

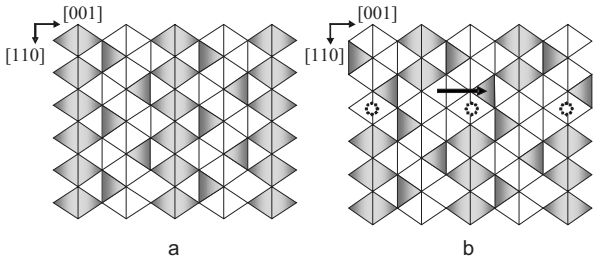

FIG. 11. Projection of the spinel structure into the $(\bar{1}10)$ plane. (a) A regular spinel arrangement with the shaded triangles and rohmbs that denote the filled tetrahedrally and octahedrally coordinated sites, respectively. Oxygen atoms are projected at the line intersections. (b) The same structure after the defect propagation. Dashed circles designate the newly formed vacant positions.

the ABO_2 layer into the $(\bar{1}10)$ plane is schematically depicted in Fig. 11(a). For simplicity, shaded triangles and rohmbs denote the tetrahedral and octahedral filled sites, respectively, while projected oxygen atoms sit at the line intersections. Since the spinel possesses cubic symmetry, the atomic sheets isostructural to ABO_2 appear in the direction perpendicular to the [110], below and above the layer drawn in Fig. 11.

If we shift one block of spinel structure with respect to the other along the ABO_2 layer on the $1/2a$ [001] vector, the anion closed packing will be restored since the oxygen positions from both parts coincide with each other after this operation. At the same time, A cations located just at the defect zone will move from the previously occupied tetrahedral sites to the similar, but earlier empty positions, as arrowed in Fig. 11(b). Consequently, corner-shared tetrahedra appear between two adjacent ABO_2 layers. It is obvious that the octahedral position nearby the fault could not be occupied due to a possible but energetically unfavorable edge-sharing contact between octahedron and tetrahedron. These vacant positions are marked with dashed circles in Fig. 11(b).

Thus, in contrast to the regular spinel structure, the gliding of ABO_2 along the planes of the {110} type causes two adjacent filled tetrahedra to be sheared through corners, while vacancies are generated in the BO_2 octahedral positions at the interface. With these newly formed vacancies or vacancy walls, AB_2O_4 stoichiometry should inevitably change. In other words, the stacking of two similar but slightly mismatched crystalline blocks of an $[Al_3O_4]^+$ structure leaves behind the layer of empty octahedra previously filled with cations and transforms the spinel arrangement of $\cdots|BO_2|ABO_2|BO_2|ABO_2|BO_2|\cdots$ into $\cdots[BO_2][ABO_2]\times[\square,O_2][A^*B^*O_2][B^*O_2]\cdots$ (here, asterisk denotes the crystalline block moved on the half-dislocation vector with respect to the other). This scenario involves the additional chain of oxygen ions just at the interface, which is very similar to the crystallographic shear defect in some transition metal oxides,[37] except for the fact that in the latter case the additional cation rather than anion positions appear and bring the nonstoichiometry to the resulting structure.

With respect to the nanodomain or building unit assumed for the description of low-temperature Al_2O_3, the above formulation produces the following consequence. The constraints of stoichiometry and the charge balance necessitate the mean thickness of the nanodomain to be not higher than two $[Al_3O_4]^+$ spinel blocks, i.e., $2[Al_3O_4]^+[2O^{2-}]2[Al_3O_4]^+$, which implies the Al_2O_3 stoichiometry. However, such a situation seems to be valid only for the fully dexydroxylated, high-temperature alumina polymorphs. For low-temperature Al_2O_3, it is quite reasonable to suggest that hydroxyl ions may occupy the newly formed anion positions between nanosized domains. If one gradually exchanges OH^- for O^{2-} in the intermediate layer formed between two mutually shifted spinel blocks, the density of such defects should inevitably grow to compensate for the charge mismatch of the hydroxyl ions. In the limited case, when the hydroxyls are fully exchanged for oxygen atoms, we arrive at the modified formulation of $[Al_3O_4]^+2[OH]^-[Al_3O_4]^+$ or $[Al_3O_4]^+[OH]^-$.

Thus, the proposed mechanism for the realization of nonstoichiometry in alumina, based on the shear defects generation, enables us to widely vary the chemical composition of alumina, which are by nature the oxyhydroxides with different concentrations of hydroxyl groups.[5,18] In a simplified way, this process can be described by

$$[Al_3O_4]OH \Rightarrow [Al_{3-(1/3)x}O_4]OH_{1-x} \Rightarrow [Al_{2(2/3)}O_4] \equiv Al_2O_3.$$

However, the crystalline chemistry representation proves more useful, namely,

$$2[Al_3O_4]OH \equiv [Al_3O_4]_2(OH)_2 \Rightarrow [Al_3O_4]_2(OH)_{2-2x}O_x \Rightarrow [Al_3O_4]_2O \equiv Al_2O_3.$$

This formulation implies that the structure and composition of the $[Al_3O_4]^+$ nanodomain do not change during dehydration and retain the ideal spinel arrangement, while hydroxyl groups associated with faults between nanodomains diffuse gradually toward the surface of the alumina particles, particularly at elevated temperatures.

Undoubtedly, formulating the low-temperature alumina derivatives as imperfect oxyhydroxides as previously proposed by Soled,[18] we could not ignore the relatively high amount of surface hydroxyl groups in these materials since prior work demonstrated this experimental fact. The structural model based on the shear defect approach considered above holds the greatest promise of clarifying the reason for the high degree of surface hydroxylation in Al_2O_3. As in the case of defect interface, the surface termination of the nonelectroneutral $[Al_3O_4]^+$ blocks could be represented by the anion layer where oxygen atoms have been exchanged for the hydroxyl ions. As a result, the surface appears populated with OH^- ions. It seem likely that these surface hydroxyls, together with OH groups associated with defects in the volume of oxide particles, may speak favorably for maintaining the electrical neutrality of the low-temperature Al_2O_3 polymorphs.

V. CONCLUDING REMARKS

This study contributes to the understanding of the reasons for the specific shapes of diffraction reflections in x-ray diffraction patterns of γ-, η-, and χ-Al_2O_3. We have presented high resolution transmission electron microscopy, x-ray pow-

der diffraction, and the simulation of the full profile diffraction patterns of low-temperature alumina polymorphs. Experimental and theoretical data are consistent with a strong faulting on the {111}, {110}, and {100} in the spinel-like structure of these materials. Stacking faults, which are the origin of the broadening of x-ray diffraction peaks, occur as individual and/or interconnecting defects on different plane families. The data obtained confirm a rather complicated microstructure of aluminas and provide strong experimental support for the description of alumina derivatives as composed of similar nanocrystalline domains comprising spinel structure. It was found that γ-, η-, and χ-Al_2O_3 differ from each other according to the crystallographic shapes of these building blocks, their way of mutual stacking, and the types of faulting arising from their assembly in an extended oxide structure. Vacancies, which are not statistically distributed point defects but ordered chains associated with the planar faulting of the crystallographic shear type that brings Al_2O_3 stoichiometry, are generated in the metastable aluminum oxides. It is highly probable that oxygen atoms are partially or completely exchanged with the hydroxyl ions in the vicinity of such defects as well as on the particle surface of low-temperature aluminas. Therefore, these materials could be considered as oxyhydroxides with variable compositions.

ACKNOWLEDGMENTS

This work was partially supported by the Russian Foundation for Basic Research (RFBR) Under Grant No. 97-03-33497. We would like to thank A. I. Ivanova and E. I. Kulko for the preparation of alumina specimens and S. V. Cherepanova for the fruitful discussion of the results. Assistance of R. Lumer with the editing of the text is highly acknowledged.

*Corresponding author; tsybulya@catalysis.ru
†Present address: GNF, Berlin-Adlershof D-12489, Germany.

[1] L. D. Hart, *Alumina Chemicals: Science and Technology Handbook* (The American Ceramic Society, New York, 1990).
[2] B. C. Lippens and J. J. Stegarda, *Physical and Chemical Aspects of Adsorbents and Catalysts* (Academic, New York, 1970).
[3] J. H. De Boer and G. M. M. Houben, *Proceedings of the International Symposium on the Reactivity of Solids, Göteburg, 1954* (Flanders Boktryckeri Aktieboolag, Göteburg, 1954), p. 237.
[4] H. Saafeld and B. B. Mehrota, Ber. Dtsch. Keram. Ges. **6**, 161 (1965).
[5] V. A. Ushakov and E. M. Moroz, React. Kinet. Catal. Lett. **24**, 113 (1984).
[6] V. Jayaram and C. G. Levi, Acta Metall. **37**, 569 (1989).
[7] R.-S. Zhou and R. Snyder, Acta Crystallogr., Sect. B: Struct. Sci. **47**, 617 (1991).
[8] M.-H. Lee, C.-F. Cheng, V. Heine, and J. Klinowski, Chem. Phys. Lett. **265**, 673 (1997).
[9] I. Levin, Th. Gemming, and D. G. Brandon, Phys. Status Solidi A **166**, 197 (1998).
[10] Y. G. Wang, P. M. Bronsveld, and J. T. M. De Hosson, J. Am. Ceram. Soc. **81**, 1655 (1998).
[11] K. Sohlberg, S. J. Pennycook, and S. T. Pantelides, J. Am. Ceram. Soc. **121**, 7493 (1999).
[12] C. Wolverton and K. C. Hass, Phys. Rev. B **63**, 024102 (2000).
[13] G. N. Kryukova, D. O. Klenov, A. S. Ivanova, and S. V. Tsybulya, J. Eur. Ceram. Soc. **20**, 1187 (2000).
[14] G. Gutierrez, A. Taga, and B. Johansson, Phys. Rev. B **65**, 012101 (2001).
[15] S.-H. Cai, S. N. Rashkeev, S. T. Pantelides, and K. Sohlberg, Phys. Rev. B **67**, 224104 (2003).
[16] C. Ruberto, Y. Yourdshahyan, and B. I. Lundqvist, Phys. Rev. B **67**, 195412 (2003).
[17] G. Paglia, C. E. Buckley, A. L. Rohl, B. A. Hunter, R. D. Hart, J. V. Hanna, and L. T. Byrne, Phys. Rev. B **68**, 144110 (2003).
[18] S. Soled, J. Catal. **81**, 252 (1983).
[19] B. C. Lippens and J. H. de Boer, Acta Crystallogr. **17**, 1312 (1964).
[20] K. J. Morrissey, K. K. Czanderna, R. P. Merrill, and C. B. Carter, Ultramicroscopy **18**, 379 (1985).
[21] M. A. Krivoglaz, *X-Ray and Neutron Diffraction in Nonideal Crystals* (Springer, Berlin, 1996).
[22] T. R. Welberry, Rep. Prog. Phys. **48**, 1543 (1985).
[23] V. A. Drits and C. Tchoubar, *X-Ray Diffraction by Disordered Lamellar Structures* (Springer, Berlin, 1990).
[24] S. V. Tsybulya, S. V. Cherepanova, and G. N. Kryukova, in *Diffraction Analysis of the Microstructure of Materials*, edited by E. J. Mittemeijer and P. Scardi (Springer, Berlin, 2004).
[25] A. S. Ivanova, G. S. Litvak, G. N. Kryukova, S. V. Tsybulya, and E. A. Paukshtis, React. Kinet. Catal. Lett. **41**, 122 (2000).
[26] E. I. Kulko, A. S. Ivanova, G. S. Litvak, G. N. Kryukova, and S. V. Tsybulya, React. Kinet. Catal. Lett. **45**, 714 (2004).
[27] D. B. Williams and C. B. Carter, *Transmission Electron Microscopy: A Textbook for Materials Science* (Plenum, New York, 1996).
[28] B. Flutz and J. M. Howe, *Transmission Electron Microscopy and Diffractometry of Materials* (Springer, Berlin, 2001).
[29] S. V. Tsybulya, L. P. Solovyeva, E. M. Moroz, and G. N. Kryukova, J. Struct. Chem. **32**, 325 (1991).
[30] P. G. Tsyrulnikov, S. V. Tsybulya, G. N. Kryukova, A. I. Boronin, S. V. Koscheev, T. G. Starostina, A. V. Bubnov, and E. N. Kudrya, J. Mol. Catal. A: Chem. **179**, 213 (2002).
[31] S. V. Cherepanova and S. V. Tsybulya, in *Proceedings of Eigth European Powder Diffraction Conference, Uppsala, 2002* (Trans Technical, Zurich, 2003), p. 87.
[32] J. Kakinoki and Y. J. Komura, J. Phys. Soc. Jpn. **7**, 30 (1952).
[33] V. I. Fadeeva, A. S. Kagan, and L. S. Zevin, Acta Crystallogr., Sect. A: Cryst. Phys., Diffr., Theor. Gen. Crystallogr. **33**, 386 (1977).
[34] J. Honstra, J. Phys. Chem. Solids **15**, 311 (1960).
[35] M. H. Lewis, Philos. Mag. **17**, 481 (1968).
[36] A. I. Ustinov, L. A. Olichovskaya, and I. M. Shmytko, Kristallografiya **45**, 408 (2000).
[37] J. S. Anderson, J. Chem. Soc. Dalton Trans. **1973**, 1107; L. A. Bursill and B. G. Hyde, Prog. Solid State Chem. **7**, 177 (1972).